ELSEVIER

Contents lists available at ScienceDirect

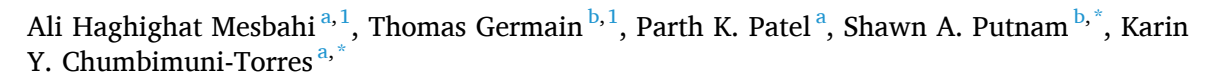
## **Applied Surface Science**

journal homepage: www.elsevier.com/locate/apsusc



Full Length Article

# Tuning the fluid wetting dynamics on gold microstructures using photoactive compounds



- a Department of Chemistry, University of Central Florida, Orlando, FL 32816-2366, USA
- <sup>b</sup> Department of Mechanical Engineering, University of Central Florida, Orlando, FL 32816-2366, USA

### ARTICLE INFO

Keywords: Surface chemistry Surface wetting Microstructured surfaces Photoreactive compounds Hemiwicking

### ABSTRACT

This work demonstrates how photoactive compounds can be used to tune the surface chemistry, surface free energy, and the wetting velocity of fluids on Spiropyran functionalized surfaces with different surface microstructures. Evidence of this photowetting effect is based on data showing: (1) the cyclic changes in the static, advancing, and receding contact angles  $\theta_{CA}$  for multiple UV $\rightleftharpoons$ vis photoswitching cycles with both smooth and microstructured surfaces and (2) the changes in the fluid wicking velocity (via UV $\rightleftharpoons$ vis photoswitching) on different Spiropyran functionalized hemiwicking surfaces. X-ray photoelectron spectroscopy is used to determine the efficiency of photoswitching caused by the quality of the Spiropyran functionalization. Reversible photoisomerization of Spiropyran generates a gradient in surface free energy, resulting in a similar change in contact angle ( $\theta_{CA}$ ) in the photoswitchable surfaces. By incorporating these changes into the Owens-Wendt and Van Oss surface energy models, the energy of smooth Au surfaces can also be predicted for both UV and visible light irradiations, where reversible contact angle variations of  $\Delta\theta_{CA} \approx 5$ –10° are achieved with both water and waterethanol mixtures due to the conversion of SP to merocyanine, which corresponds to a total free energy change of  $\sim$ 13% on the photoswitchable surface.

## 1. Introduction

Researchers have studied the dynamics of surface wetting over the past century to better understand the interaction between liquids and solids [1–2]. Studying these interactions is essential for a variety of applications, ranging from biomedical devices to self-cleaning surfaces [3–4]. The contact angle ( $\theta_{CA}$ ) is a parameter commonly used to characterize the wetting behavior and the energetics of the solid/liquid interface (Fig. 1). Numerous attempts have been made to model the wetting behavior using  $\theta_{CA}$ , most famously through the Young-Dupree Equation [5–6]:

$$\cos\theta_{\rm Eq} = \frac{\gamma_{\rm sv} - \gamma_{\rm sl}}{\gamma_{\rm lv}} \tag{1}$$

where  $\theta_{\rm Eq}$  represents the static or equilibrium contact angle and  $\gamma_{\rm lv}$ ,  $\gamma_{\rm sv}$  and  $\gamma_{\rm sl}$  are the liquid–vapor, solid–vapor, and solid–liquid interfacial surface energies, respectively [6]. It is worth mentioning that the surface

free energy  $(\gamma)$  and surface tension  $(\sigma)$  were related by Shuttleworth [7] through the following equation:

$$\sigma = \gamma + A \frac{d\gamma}{dA} \tag{2}$$

where A is surface area,  $\sigma$  is the surface tension, and  $\gamma$  is the interfacial or surface Helmholtz free energy per unit area. For a one-component fluid, the  $d\gamma/dA$  term is negligible and, in result,  $\gamma$  and  $\sigma$  are often assumed to be equivalent - which is not necessarily accurate, especially for solids.

The magnitude of  $\theta_{CA}$  is most commonly used to describe the lyophilicity ( $\theta_{Eq} < 90$ ) or lyophobicity ( $\theta_{Eq} > 90$ ) of a surface material. With respect to aqueous fluids [8–10], the degree of hydrophilicity or hydrophobicity is then subsequently used to predict if a surface material is suitable for aqueous self-wetting or self-cleaning applications, respectively. Fig. 1(a) shows the schematic of a water droplet on a hydrophobic surface. The wetting behavior of a surface can also be tuned by surface texturing with micro- to nano-scale surface structures [11–13]. To create

E-mail addresses: Shawn.putnam@ucf.edu (S.A. Putnam), Karin.ChumbimuniTorres@ucf.edu (K.Y. Chumbimuni-Torres).

<sup>\*</sup> Corresponding authors.

<sup>&</sup>lt;sup>1</sup> Authors with equal contribution.

a self-drying surface, microstructures are used to increase the hydrophobicity of a naturally hydrophobic surface [14]. Similarly, microstructures can also be used to increase the hydrophilicity of a naturally hydrophilic surface to create a self-wetting surface [15]. Fig. 1(b)-(d) illustrate three key fluid wetting behaviors with microstructured surfaces. A Cassie-Baxter state (Fig. 1(b)) occurs when the microstructures of a hydrophobic surface material prevent a fluid from wetting the entire surface. For example, the hydrophobic nature of the surface chemistry and the gradient of surface energy created by the air pockets in the microstructure array will prevent the liquid from reaching/wetting the substrate. Instead, the liquid will only rest on top of the microstructures [16]. The Wenzel state (Fig. 1(c)) describes a condition where the liquid rests within the microstructure array as a droplet but does not spread throughout it. This state can occur for both hydrophobic and hydrophilic surfaces [17]. Lastly, the hemiwicking state (Fig. 1(d)) describes the movement (wicking) of fluid through the surface textures of a hydrophilic surface material induced by a cascading, capillary force effect with each microstructure (i.e., each micropillar acts as a fluid pump and a fluid droplet can wet a surface beyond its equilibrium wetting length). Some common applications for hemiwicking include thermal control systems, such as heat pipes [18].

While multiple research groups have demonstrated systems that can exhibit wetting transitions between the Wenzel and Cassie-Baxter states [19–21], an active tuning between the static Wenzel (or Cassie-Baxter) state to the dynamic hemiwicking state has yet to be demonstrated. It is important to note that the difference between the static and dynamic wetting characteristics are dependent on multiple parameters, including the advancing and receding contact angles, the geometry of the surface texture, the presence of surface energy gradients (intrinsic and/or induced), and the absorption kinetics. Nevertheless, the ability to actively switch between the Cassie-Baxter, Wenzel, and Hemiwicking states will lead to transformative fluidic technologies - especially if the wetting state transitions can be controlled by contact-free stimulants such as light.

A variety of approaches have been proposed to control the wetting dynamics in different applications by tuning the interfacial properties both actively and passively. The use of oxides, for example, has been investigated with nucleate boiling heat transfer to increase wetting speeds (and, therefore, increase the critical heat flux) in thermal management applications [22–24]. Moreover, external stimuli such as temperature [25–27], electricity [28–29], pH [30], and solvent [31] were used to modulate the wetting dynamics on various surfaces. For example, various methods have been reported to improve the controllable wettability of  $\text{TiO}_2$ -derived materials and their applications [32]. There have also been considerable attempts to tune the wettability with

organic photochromic compounds (OPC) toward photoswitchable surfaces (Azobenzene [33–39], Spiropyran (SP) [40–42], and Donor-Acceptor Stenhouse Adducts (DASA)) [43].

OPCs are a class of photoactive compounds that undergo reversible structural transformation of their physicochemical properties (i.e., polarity and charge distribution) upon light irradiation (photoisomerization) as an external stimulus [44,45]. For passive applications, photoswitching with light is advantageous because it is abundant and inexpensive. Moreover, for active applications, the wavelength, power, and spatiotemporal characteristics of the light stimulus can be easily controlled. Among the OPCs, SP is one of the most used compounds and it has been attached to polymers, biomacromolecules, and inorganic nanoparticle surfaces [46,47].

The main goal of this research is to address the dynamic range of tuning thewetting behavior of surfaces functionalized with photoactive SP compounds. Variations in the static and dynamic (advancing and receding) contact angles are analyzed with both smooth and microstructured Au surfaces functionalized with SP to access the possibility of reversible switching between the static Cassie-Baxter (or Wenzel) state and the dynamic hemiwicking state. The wetting behaviors of multiple fluids with varying polarity (ethanol-water mixtures) are also studied. Based on the variation in surface free energy, these changes are both measured and predicted for water, ethanol, and binary water/ethanol mixtures. The surface chemistry is modulated by light irradiation, which can alter the surface energy and wetting behavior of the photoswitchable Au (SP-SAM). The study provides preliminary results for designing microstructured surfaces with tunable surface free energy perturbations via the photoisomerization of SPCOOH surface coatings.

#### 2. Experimental setup

## 2.1. Synthesis of SPCOOH

The synthesis of SPCOOH consists of two steps. In the first step, we proposed a new synthesis method for 1-(2-carboxyethyl)-2,3,3-trimetyl-3H-indolium bromide, which functions as a SPCOOH precursor. In the second step, SPCOOH is synthesized by modifying a literature procedure (details are presented in the supplementary information (Scheme S1, Fig. S1 and S2)).

## 2.2. Creating the microstructured surface

The change in the wetting behavior is analyzed from contact angle experiments with both flat (smooth) Au and microstructured Au sample substrates. Commercially available flat Au substrates were obtained

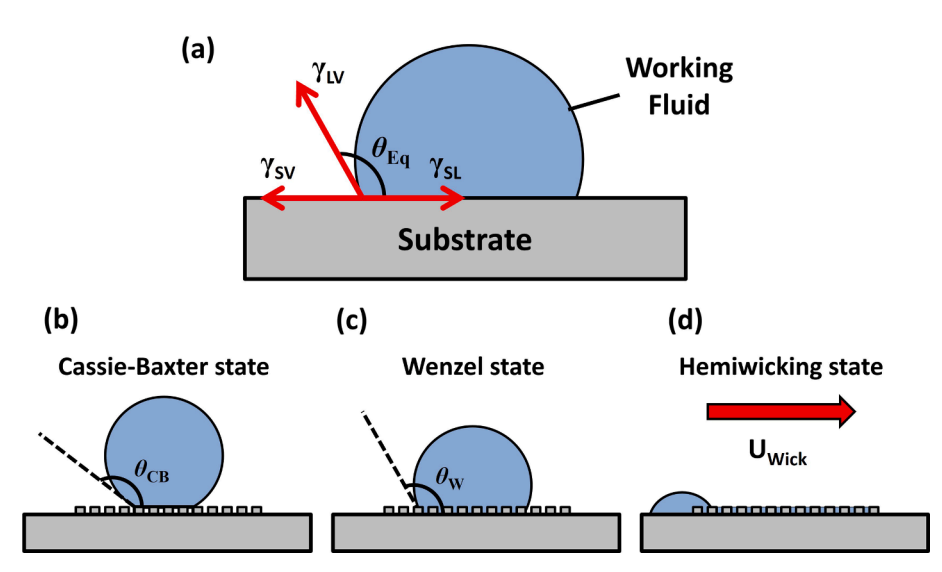


**Fig. 1.** A representation of the interfacial forces forming the contact angle of a fluid on **(a)** a flat hydrophobic surface and **(b-d)** microstructured surfaces for the Cassie-Baxter, Wenzel, and Hemiwicking wetting states, respectively. The contact angles depicted for the **(b)** Cassie-Baxter and **(c)** Wenzel states are the apparent contact angles for the textured surface, where  $\theta_{CB} > \theta_W > \theta_{Eq}$  and  $\theta_{Eq}$  is the corresponding equilibrium contact angle for the same fluid on the flat (non-textured) surface region.

**Table 1** Pillar packing orientation, shape, geometry (base diameter d, height h, spacing  $s_x$ , skew  $\alpha$ , slant  $\beta$  angle), and roughness factor  $f_r$  of the microstructured hemiwicking samples used in this study.

| Sample | Orientation | Shape         | d (μm) | h (μm) | $s_x$ ( $\mu$ m) | $\alpha$ (deg) | $\beta$ (deg) | $f_r$ |
|--------|-------------|---------------|--------|--------|------------------|----------------|---------------|-------|
| 1      | Staggered   | half-Cylinder | 20     | 17.5   | 40               | 45             | 0             | 1.28  |
| 2      | Cubic       | Crescent      | 20     | 20     | 50               | 0              | 0             | 1.46  |
| 3      | Cubic       | half-Cylinder | 30     | 25     | 50               | 0              | 0             | 1.77  |
| H      | Cubic       | half-Conical  | 20     | 44     | 50               | 0              | 12.8          | 1.46  |
| G      | Staggered   | half-Conical  | 30     | 97     | 40               | 45             | 8.8           | 2.18  |
| K      | Cubic       | half-Conical  | 30     | 58     | 50               | 0              | 14.5          | 1.91  |

from Infolab, Inc. Two methods were used to fabricate Microstructured Au substrates. The first method is based on our previous work to fabricate microstructured substrate surfaces in a timely and cost-effective manner using a negative mold methodology [48]. A microstructured surface is created by curingpolydimethylsiloxane (PDMS), Norland optical adhesive 61 (NOA), or JB-Weld on a negative, micro-patterned plastic mold. DC magnetron sputtering is then used to deposit a ~100 nm thick, thin film of Au on the cured, micro-structured material samples. The second method involves polymerization using a Nanoscribe Pro GT laser lithography system to fabricate microstructures on a silicon wafer (thickness = 0.5 mm). These microstructures on Si are then coated with a thin, protective layer of  $Al_2O_3$  (~150 nm) to maximize robustness and surface energy uniformity. These microstructured samples (or anisotropic hemiwicking arrays) were fabricated at the Center for Nanophase Material Sciences at Oak Ridge National Laboratory (ORNL). Then, ~100 nm of Au is deposited on the protective Al<sub>2</sub>O<sub>3</sub> surface coating (via DC magnetron sputtering). Table 1 provides a summary of the geometries of the microstructured wicking arrays used in this study.

### 2.3. Fabrication of photoswitchable surfaces

Fig. 2 illustrates the two steps required to prepare SP functionalized surfaces on both the flat and microstructured Au sample substrates. Initially, the Au substrate is immersed in a 5 mM solution of cystamine dihydrochloride for 48 h to produce a self-assembled monolayer (SAM) containing a terminal amino group. The SAM functionalized Au is then rinsed with DI water and placed in an ethanolic solution containing 5 mM carboxylated SP (SPCOOH) and 1 mM 1-Ethyl-3-(3-dimethylamino-propyl) carbodiimide (EDC) and left in the solution overnight. A condensation reaction occurs between the amino groups of cystamine

and the carboxylic acid groups of SPCOOH, resulting in an SP-functionalized Au surface (SP-SAM). The surface chemistry of SAM and SP-SAM attached to the Au surface was analyzed using X-ray photoelectron spectroscopy (XPS). The XPS experiments were conducted using a Physical Electronics 5400 Electron and Spectroscopy for Chemical Analysis (ESCA).

#### 2.4. Photoswitching experiments

The photoswitchable Au substrate undergoes a ring opening of SP (MC) with UV light irradiation and switches back to the closed form of SP with visible light irradiation (Fig. 2(b)). The ring opening of SP produces positive charges in nitrogen and negative charges in oxygen. UV-AC hand lamps ( $\lambda=365$  nm) and a 120 LED array ( $\lambda=520$  nm) were used to induce the ring opening and closing of SP, respectively. The wavelengths were selected based on the absorption experiments with SPCOOH in ethanolic solution detailed in the Supplementary Information (Fig. S3 and S4). Based on these experiments, one minute of UV irradiation is optimized for the photoisomerization of SP into merocyanine (MC) and ten minutes of visible irradiation for the reverse reaction (MC into SP). The photoswitching experiments were conducted in three cycles.

## 2.5. CA measurements

Fig. 3 illustrates the wetting experiment for photoswitchable surfaces measured by contact angle analysis using a VCA-Optima surface analysis (AST Products, Billerica, MA). Using a computer-controlled syringe pump, a droplet of 6  $\mu$ L of water was dispensed on the surface and an image of the static droplet was captured. In addition to the static contact

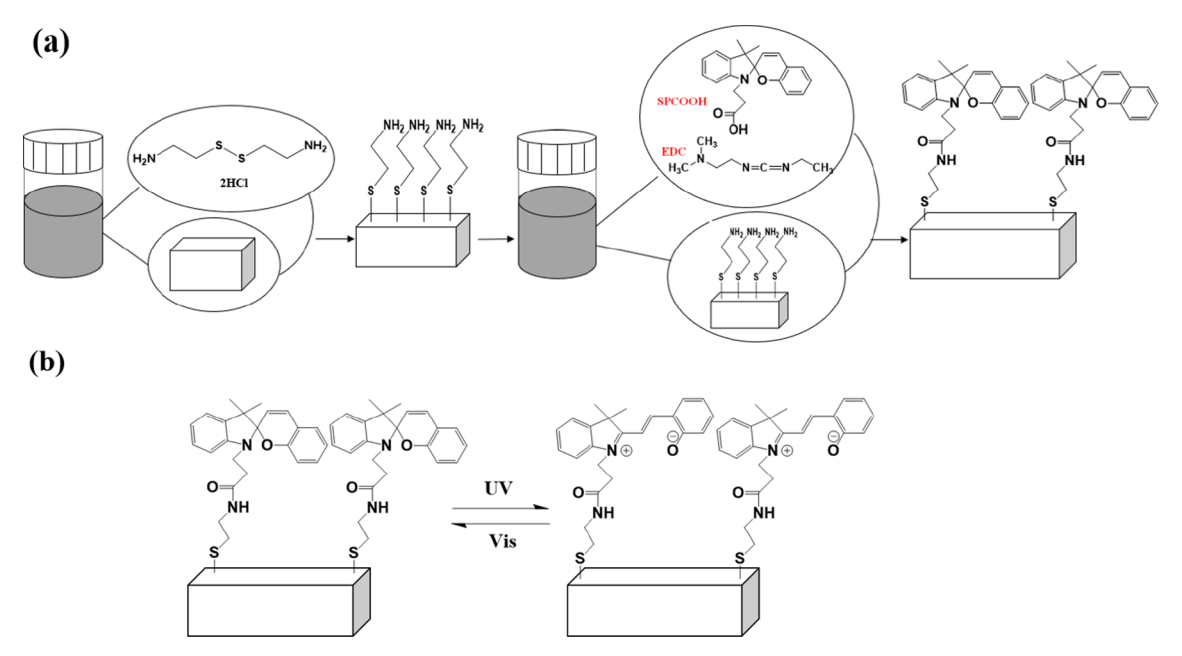


Fig. 2. The process for (a) functionalization of cystamine and SPCOOH onto an Au substrate (b) photoisomerization of SP on the Au substrate.

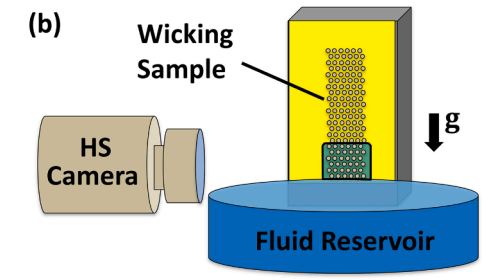


Fig. 3. (a) Schematic depiction of the surface wetting apparatus for measuring the advancing, receding, and static contact angles. (b) Schematic depiction of the vertical hemiwicking apparatus.

angle, the VCA instrument was used to measure the advancing and receding contact angles. The advancing angle was captured by placing a droplet on a surface and then adding fluid to the droplet (increasing its volume and contact angle), until the droplet's contact/triple line "depins" from the surface and then advances along the surface to a value close to the droplet's equilibrium contact angle. Thus, the advancing contact angle corresponds to the contact angle at the inception of "depinning". A similar method was used to capture the receding angle, but the syringe was used to remove fluid from the droplet (reducing its volume and contact angle) until de-pinning occurs. Video recordings by the camera capture the droplet dynamics for these advancing and receding experiments (Fig. 3(a)). The contact angle measurments were performed using a red-light lamp ( $\lambda \approx 780$  nm) since it does not affect the structure of SP as shown by the absorption plots in the Supplementary Information (S4). In between successive trials and other subsequent experiments, the samples were cleaned with DI water and dried with nitrogen gas.

#### 2.6. Hemiwicking

The hemiwicking experiments were performed on functionalized SP microstructures to determine the effects of wetting state transitions for different 'light-induced' variations in surface energy, changes in fluid composition, and variations in surface texture. A high-speed camera (Fig. 3(b)) was used to capture the hemiwicking dynamics of ethanol/ water mixtures (25:75, 50:50 and 75:25 vol% of ethanol:water, respectively). The hemiwicking experiments investigated the both the 'open' and 'closed' SP-states. The 75:25 mixture has the smallest surface tension, making it more likely to wick while retaining its polarity. The presented data are based on vertical wicking experiments (against gravity) using a vertical translation stage (Fig. 3(b)), where a solution reservoir was moved up to the hemiwicking sample until it met the firstrow pillars in the hemwicking pillar array. The hemiwicking process starts at the onset of fluid meniscus contact with the pillar array. The wicking dynamics were captured at 100 frames per second (fps) at an image resolution of 14.71 µm/pixel. Similar to the contact angle experiments, after UV ( $\lambda = 365 \text{ nm}$ ) or vis ( $\lambda = 520 \text{ nm}$ ) light exposure, the hemiwicking dynamics were monitored by the high-speed camera using a red-light lamp ( $\lambda \approx 780$  nm) for visual purposes since it does not affect the structure of SP. Horizontal wicking experiments from droplets (representative of Fig. 1(d)) were also conducted. However, with this horizontal configuration we did not observe hemiwicking or, more importantly, UV ≥vis photoswitching transitions between the Wenzel (or Cassie-Baxter) state and the hemiwicking state.

#### 3. Results and discussion

## 3.1. Advancing, receding, and static CA with water

Fig. 4 shows the changes in the static and dynamic contact angles for water on the SP functionalized flat Au sample for three UV ≥vis

photoswitching cycles. Under UV-light radiation,  $\theta_{CA}$  (static and dynamic advancing/receding) decreases due to the photoisomerization of hydrophobic SP to hydrophilic MC (see Fig. 2(b)).

The static  $\theta_{CA}$  changed by approximately  $10^{\circ}$ , which is comparable to previous studies [33,37–40] and decreased over the second and third cycles due to SP photodegradation during exposure. In fact, Spiropyran photoisomerization is associated with some side reactions. These reactions can lead to by-products that lack the photoresponsive properties [46]. One of the most important mechanisms for these side reactions is due to the interaction between the long-lived triplet excited state of SP with the triplet oxygen ( $^{3}$ O2). This generates a singlet oxygen ( $^{1}$ O2) which initiates irreversible oxidation of the photoswitching process [46].

The dynamic  $\theta_{CA}$  were also used to determine changes in the wetting dynamics in a non-equilibrium state, since these contact angles are tied to  $d\gamma/dA$  (Eq. (2)) and heterogeneities in surface energy. The advancing contact angle results in Fig. 4 show comparable switches in the magnitude as that measured for the static contact angle, while the receding contact angle data show a lower degree of photoswitchability. Nevertheless, for all conditions (static and dynamic), the behavior of the photoswitching shows that changes in the surface chemistry result in variations in the solid/liquid interface (Fig.S5 and Table S1). We hypothesize that these changes in the advancing and receding angles will tune the fluid wetting dynamics on the SP functionalized Au substrate, proving that SP reversibly changes the apparent hydrophobicity of the Au microstructured surface. This capability to tune the fluid wetting dynamics has broader impacts in heat transfer and self-cleaning applications.

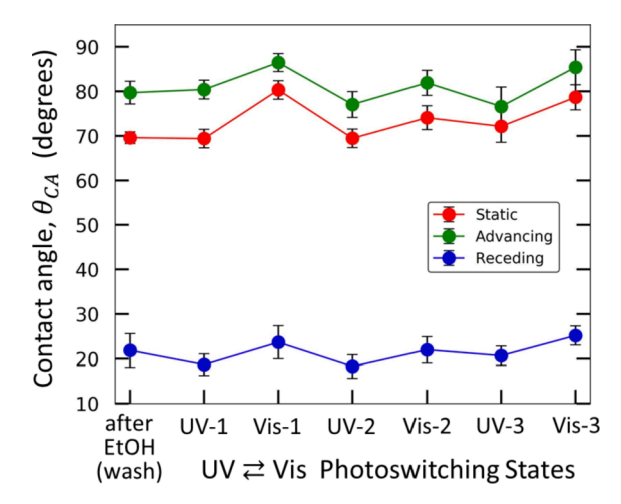


Fig. 4. The static, advancing, and receding contact angles verses the imposed UV ⇒vis light irradiation cycles with water droplets on a flat Au substrate functionalized with the photoactive SPCOOH compound.

#### 3.2. Composition of photoswitchable surface

XPS was conducted to determine the composition of the SAM and SP-SAM on the switchable surface. Six spots (surface locations) were selected for XPS analysis of the SAM and then the SP-SAM surface chemistries. The results are presented in Table 2 and Fig. 5.

Carbon is the most abundant element on the SP-SAM surface, followed by oxygen, nitrogen, and Au. The C 1s spectrum (binding energy ranging ~282–286 eV) is the result of the formation of SAM using C—C: 284.8 eV, C-S bond: ~284.5, C-N: ~285.5, C-Cl: ~285.2, C-H  $\sim$ 286 eV and formation of SP-SAM C—O—C:  $\sim$  286 eV. The N 1s region (binding energy ~397-400 eV) shows the formation of SAM (peaks at ~399.5 and ~400.8 eV can be attributed to the N-H and N-C, respectively). The O 1s spectrum (binding energy ~529-533 eV) confirms the oxidation of both the SAM and SP-SAM surfaces. SAM induces oxidation of the thiol groups formed upon adsorption of cystamine. This process produces either  $SO_3^-$  ions or  $SO_2^-$  groups, which desorb from the Au surface. Furthermore, the oxidation can be caused by multiple factors, including prolonged immersion times, oxygen in the SAM solution, air exposure, and photooxidation of the photoswitchable surface by UV exposure [49]. Also, the oxidation process occurs during samples preparation for XPS as well as during the photoswitching experiment. Oxidation can decrease photoswitching on surfaces by washing out the SAM and SP-SAM with a polar solvent, such as water (during experi-

Quality control of SAM and SP-SAM is imperative to increase the overall performance of photoswitchable surfaces. Highly aligned SAMs, theoretically, can contain higher terminal amino group packing densities. The ideal carbon to nitrogen molar ratio is  $[C/N] \sim 2$ , maximizing the possibility of a condensation reaction between the terminal amino atom of SAM and the carboxylic acid group of SPCOOH. Thus, ideal alignment results in a higher density of SP-SAM on the surface. As shown in Table 2, the carbon to nitrogen molar ratio [C/N] in the SAM is  $\sim 17$  ( $\sim 8$  times greater than the theoretical value of 2), which suggests that either the fabricated SAM is not well aligned or there is airborne molecular contamination (adventitious carbon) [50,51]). The lack of surface coverage and non-ideal alignment are presumably the primary causes of a partially covered and misaligned SAM.

Several important factors contribute to the formation of SAM, such as immersion time and cystamine concentration in the SAM solution [52,53]. The SAM in the photoswitchable surface was formed by immersing the Au substrate in 5 mM cystamine dihydrochloride solution over 48 h (1–10 mM and 1–24 h are prevalent ranges for SAM formation [54–56]). Results showed that 5 mM of cystamine dihydrochloride provides superior photoswitching in comparison to a higher concentration of 7.5 mM (Fig. S6). Extended immersion times have a contradictory effect. On the one side, increasing surface coverage of SAMs results in fewer defects. On the other side, prolonged immersion times are associated with an increase in the amount of oxidized carbon and sulfur in the photoswitchable surface [50]. The 12.68% of the oxygen in the SAM is composed mainly of oxidized carbon and sulfur. Oxidized sulfur may result in the detachment of the SAM from the Au surface and a decrease in the switching performance.

Besides the SAM, the SP-SAM structure and quality have an important impact on the wetting behavior of the photoswitchable surface.

**Table 2** Element composition on the Au surface.

| Element | Atomic % |                                  |  |  |  |
|---------|----------|----------------------------------|--|--|--|
|         | SAM      | Photoswitchable surface (SP-SAM) |  |  |  |
| C, 1s   | 52.82    | 66.54                            |  |  |  |
| O, 1s   | 12.68    | 14.2                             |  |  |  |
| N, 1s   | 3.1      | 9.18                             |  |  |  |
| Au, 4f  | 28.8     | 8.05                             |  |  |  |
| S, 2p   | 2.6      | 2.03                             |  |  |  |

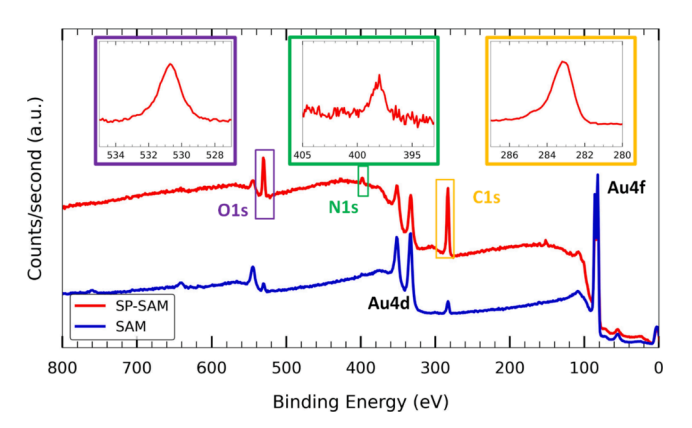


**Fig. 5.** XPS spectra after formation of (1) SAM (blue), (2) SP-SAM on a flat Au substrate. (For interpretation of the references to colour in this figure legend, the reader is referred to the web version of this article.)

First, the SP-SAM quality is reduced by the presence of bulky SP groups in the formation procedure. Sterically bulky SPs inhibit the development of densely packed SP-SAMs and result in a disordered SAM [50]. Second, the formation reaction of SP-SAM is incomplete (amino groups in the 398–400 eV region of the XPS spectrum (Fig. 5)). This reduces the number of attached SP to the Au and consequently its photoswitching performance. And finally, photodegradation of SP upon UV irradiation leads to a decrease in  $|\Delta\theta_{CA}|$  after repeated UV $\rightleftarrows$ vis photoswitching cycles (see Sec. 3.1).

#### 3.3. Results of ethanol-water mixture and surface energy analysis

The free surface energy variation between the 'open' and 'closed' form of SP is due to the different types and magnitudes of intermolecular interactions [57]. This variation mainly comes through the exposure of the positive and negative charges in the open state (i.e., after UV light exposure) and the structure with no free charges in the closed state (i.e., after visible light exposure). For this study, the Owens-Wendt and the Van Oss Chaudhury Good models were used to predict the surface energy variations of the photoswitchable surface upon UV or vis light irradiation. These two surface energy models consider the polar and nonpolar contributions of the liquid and the solid surface energy to predict the contact angle. The Owens-Wendt model, which is closely related to Fowke's Theory, can be expressed through the following equation [58]:

$$\frac{1 + \cos\theta_{CA}}{2} \frac{\gamma_l}{\sqrt{\gamma_l^d}} = \sqrt{\gamma_s^p} \sqrt{\frac{\gamma_l^p}{\gamma_l^d}} + \sqrt{\gamma_s^d}$$
 (3)

where  $\gamma_l$  is the surface energy of the fluid,  $\gamma_s$  is the solid surface energy,  $\gamma^p$  is the polar component of the surface energy, and  $\gamma^d$  is the non-polar component of the surface energy. The Van Oss Chaudhury Good model, or simply Van Oss model, analyzes the wetting through two different aspects of the polar surface energy, the electron accepting (acid,  $\gamma^+$ ) and the electron donating (base,  $\gamma^-$ ) components. In relation to the polar component of surface energy, the acid and base contributions are given by the following equation [58]:

$$\gamma^p = 2\sqrt{\gamma^+ \gamma^-} \tag{4}$$

Using this contribution, the Van Oss model calculates surface wetting using [59]:

$$(1 + \cos\theta_{CA})\gamma_l = 2\left(\sqrt{\gamma_s^d \gamma_l^d} + \sqrt{\gamma_s^+ \gamma_l^-} + \sqrt{\gamma_s^- \gamma_l^+}\right)$$
 (5)

Data from the ethanol and water experiments can be used to find the surface energy components using both the Owens-Wendt and Van Oss models. A proper application of the Van Oss model requires, however, an

estimate of the surface energy. An approximation for the total surface energy is provided through the Chimbowski method, which is presented in the following [60]:

$$\gamma_s = \Pi \frac{(1 + \cos\theta_{adv})^2}{(1 + \cos\theta_{rec})^2 - (1 + \cos\theta_{adv})^2} \tag{6}$$

where  $\Pi$  is the film pressure between the thin, absorbed film layer of a fluid and the surface.  $\Pi$  can be calculated using the following equation:

$$\Pi = \sigma(\cos\theta_{rec} - \cos\theta_{adv}) \tag{7}$$

The data from the dynamic contact angle experiments with water are used to find the solid surface energy. The polar and non-polar components of the surface energy are then related through the following equation [61]:

$$\gamma = \gamma^p + \gamma^d \tag{8}$$

To verify the surface energy values, both the theoretical and experimental contact angles of the ethanol/water mixtures are compared at different volume fractions  $\phi$  (for both the 'open' and 'closed' forms of SP on the photoswitchable surface). The surface energy of the fluid mixtures for the Owens-Wendt and Van Oss models are estimated using effective medium theory (EMT), e.g.,

$$\sigma_{mix} = \sum_{i}^{N} \phi_{i} \sigma_{i} \tag{9}$$

Eqs. (1)–(9) are then used to calculate the changes in the surface free energy based on the wetting data gathered for both water, ethanol, and water-ethanol mixtures. Additional details regarding the properties of the fluid mixtures are provided in the Supplementary Information (Figs. S7 and S8).

Table 3 provides our results for the different surface free energy contributions. Using these calculated surface energy values, Fig. 6 then summarizes our results in terms of  $\theta_{CA}$  measured and  $\theta_{CA}$  predicted based on the different surface free energy contributions provided in Table 3. Despite minor differences in the surface energy values, both models can approximate the value of the surface energy and its overall changes rather well. Moreover, as illustrated in Fig. 6, the experimental results for pure ethanol ( $\phi = 0$ ) and pure water ( $\phi = 1$ ) were rather accurate for predicting  $\theta_{CA}$  of the water/ethanol mixtures. According to the Van Oss model, there is a 12.84% increase in the total free surface energy upon photoisomerization of closed form SP state to the open form MC state. Thus, both the experiment results and the surface energy modeling indicate that the overall increase in free surface energy is primarily due to an increase in the polar surface energy component which is caused by the presence of the positive and negative charges in the open (MC) state. These findings also support that the surface charge (polarity) causes the primary changes in the surface free energy resulting in the expected overall change in the wetting behavior (or  $\theta_{CA}$ 

**Table 3**Surface energy components for water, ethanol, and the photoswitchable SP functionalized Au surface, using the Owens-Wendt and Van Oss Models [58–64] for the UV light ('open') and vis light ('closed') photoswitching states.

| Material                            | σ*,<br>γ(mN/m) | γ <sup>d</sup> (mN/<br>m) | γ <sup>p</sup> (mN/<br>m) | γ <sup>+</sup><br>(mN/<br>m) | γ <sup>-</sup><br>(mN/<br>m) |
|-------------------------------------|----------------|---------------------------|---------------------------|------------------------------|------------------------------|
| Water                               | 72.8*          | 21.8                      | 51                        | 25.5                         | 25.5                         |
| Ethanol                             | 23.2*          | 21.4                      | 1.8                       | 0.09                         | 9.0                          |
| SP-Au, Closed (vis),<br>Owens-Wendt | 31.14          | 9.51                      | 21.63                     | -                            | -                            |
| SP-Au, Open (UV),<br>Owens-Wendt    | 34.79          | 8.40                      | 26.39                     | -                            | -                            |
| SP-Au, Closed (vis),<br>Van Oss     | 29.84          | 8.96                      | 20.88                     | 7.27                         | 14.99                        |
| SP-Au, Open (UV),<br>Van Oss        | 33.67          | 7.34                      | 26.34                     | 9.13                         | 19.00                        |

as a function of the UV ≥ vis light stimulation).

The Van Oss model can provide a better understanding of the changes in the polar component of the surface energy. As mentioned earlier, the Owens-Wendt model only considers the total polar component of surface energy, while the Van Oss model analyzes the acid-base component of surface tension. Positive and negative charges exposed in the 'open' SP state are representative of the nitrogen and oxygen molecules, respectively (see Fig. 2(b)). Based on the Van Oss models, it is observed that the main changes in the polar component of the surface energy are caused by the electron donating (i.e., base) component. This indicates that the negative charges on oxygen molecules in the 'open' SP state are more influential in altering the overall surface free energy than the positive charges on nitrogen molecules.

#### 3.4. The impact of surface microstructure

#### 3.4.1. Cassie-Baxter, Wenzel, and Hemiwicking state

Fig. 7(a) shows the measured changes in  $\theta_{CA}$  of water droplets for three UV zvis irradiation cycles with two different photoswitchable surfaces (flat and microstructured). Fig. 7(b) provides data for waterethanol mixtures on both flat (filled circle symbols) and microstructured (open triangle symbols) Au surfaces functionalized with SP. Similar to the  $\Delta \theta_{CA}^{\mathrm{UV} \rightleftarrows \mathrm{vis}}$  modulations observed for the smooth (flat) SPfunctionalized Au surface, the apparent  $\theta_{CA}$  for the microstructured pillar array varies depending on the SP state of the photoactive compound. Thus, photoisomerization of the SP 'closed' state to MC 'open' state not only alters the intrinsic surface free energy of the functionalized Au surface, but also modulates the capillary force coupled to the surface texture of the microstructure. While the photoactive compound only facilitates relatively small modulations (i.e.,  $\Delta \theta_{CA}^{UV \rightleftharpoons vis} \approx 5 - 10^{\circ}$ ), the tunability of  $\theta_{CA}$  is repeatable and still offers preliminary results towards the design of systems that can exhibit this photowetting effect with both textured and non-textured surfaces. Moreover, these results support the broader impacts of potentially using other OPCs for tunable wetting beyond that for flat surfaces, where the wetting dynamics can be controlled/tuned by engineering both the surface microstructure and the surface photochemistry.

Multiple researchers have derived criterion for predicting the different wetting states and wetting state transitions [65-70]. Most commonly conventional wetting theory [67] is used, where it can predict the apparent contact angle for all three wetting states based on the geometry of the surface microstructure, the fractional wetted area, and the equilibrium contact angle of the intrinsic surface material without microstructures. For the Wenzel state (Fig. 1(c)), conventional theory predicts the apparent Wenzel state contact angle  $(\theta_W)$  to follow as  $\cos\theta_W = f_r \cos\theta_{CA}^*$ , where  $\theta_{CA}^*$  represents the equilibrium contact angle for the non-textured (flat) surface and  $f_r$  is the roughness factor (i.e., the ratio of the total surface area of the microstructured surface to the projected surface area). On the other hand, the apparent Cassie-Baxter contact angle ( $\theta_{CB}$ ) for the traditional, air-pocket wetting regime (Fig. 1(b)) can be expressed as  $\cos\theta_{CB} = \Phi(\cos\theta_{CA}^* + 1) - 1$ , where  $\Phi$  is the fraction of the wetted solid surface area to the projected surface area. Based on these wetting state predictions, the photo-induced changes in  $\theta_{CA}$  for water with microstructured sample in Fig. 7(a) corresponds to slight perturbations in an unstable Cassie-Baxter wetting state with  $98^{\circ}$  $\lesssim\!\!\theta_{CB}\!\lesssim108^\circ$ , using  $\Phi\approx0.5$ –0.7 and  $\theta_{CA}^*\approx67$ –85 $^\circ$  based on the bare Au photoswitching results. Therefore, with further enhancements in the photoisomerization of the SP surface coating, a Cassie-Baxter to Hemiwicking (or droplet penetration) state transition is feasible. For example, if UV light stimulation can reduce the apparent Cassie-Baxter contact angle with water to the hydrophilic state (i.e.,  $\theta_{CB} \leq 90^{\circ}$ ), then the Cassie-Baxter to Hemiwicking state transition should occur via a cascading Cassie-Baxter to Wenzel to hemiwicking transition. Equivalently, reversible Cassie-Baxter to Hemiwicking transitions are expected with water if UV ≥ vis stimulation can induce the corresponding intrinsic

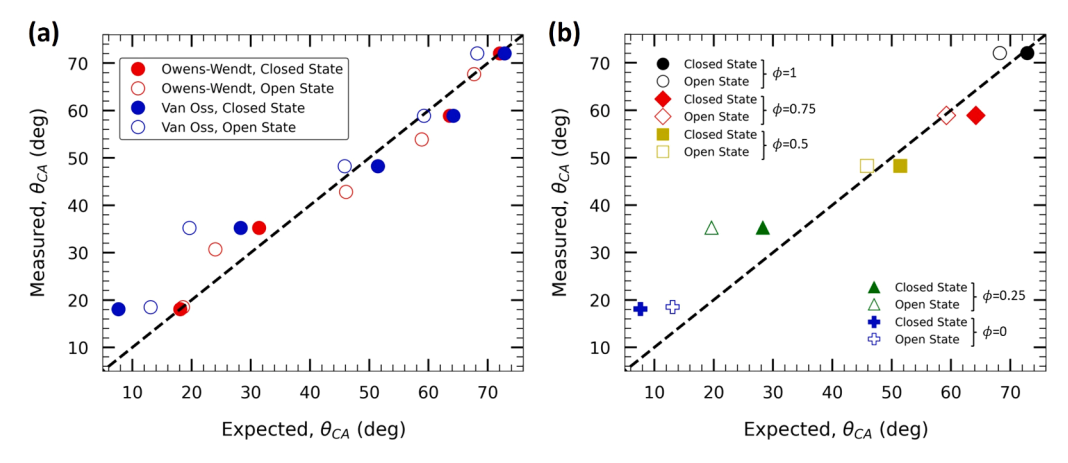


Fig. 6. Comparison of the theoretical and experimental contact angles for water, ethanol, and water/ethanol mixtures using (a) the Owens-Wendt (Eq. (1)) and the Van Oss (Eq. (3)) wetting models and (b) variations in the water volume fraction derived from the Van Oss model.

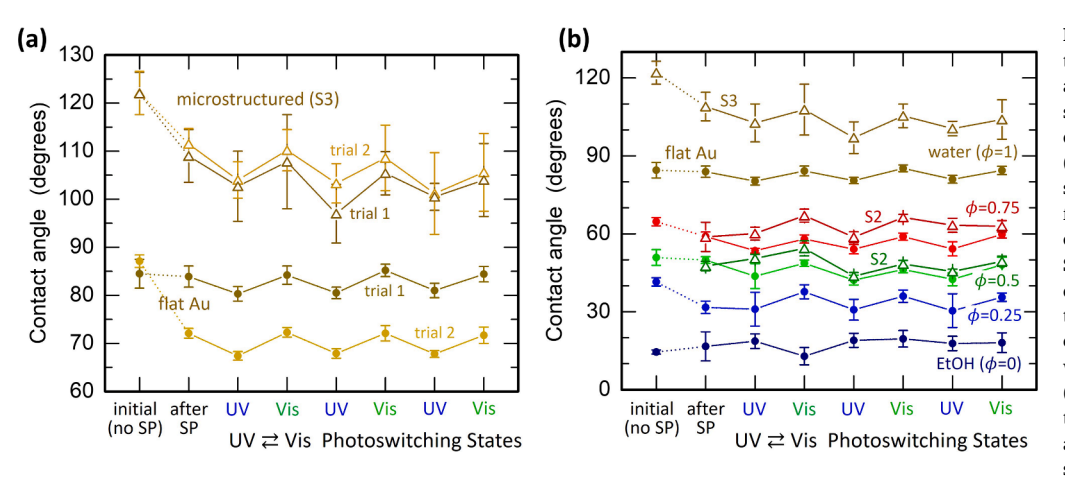


Fig. 7. The effects of SPCOOH functionalization, surface microstructure, and UV ≥vis photoswitching on the static contact angle. (a) Contact angle data for water droplets on both bare (smooth) Au and microstructured Au surfaces before and after SPCOOHfunctionalization and then with subsequent UV ≥ vis photoisomerization of the SP surface coating. (b) Contact angle data for different water-ethanol mixtures. The circle symbols (o) represent equilibrium contact angles for water (or water-ethanol mixtures) on the smooth (non-textured) Au surface, whereas the triangle symbols ( $\triangle$ ) represent the apparent contact angles for a microstructured sample surface - (a) Sample-3 and (b) Sample-2 (see Table 1). The initial (no SPCOOH) data points corre-

spond to the contact angles measured with the untreated Au surface (i.e., before the Au surface was functionalized with the photoactive SPCOOH compound). The data are based on multiple experiments (5 minimum per data point), where (a) provides data for multiple trials.

(flat surface) contact angle conditions:  $\theta_{CA}^{UV} \leq 40^\circ$  and  $\theta_{CA}^{vis} \geq 90^\circ$ . This  $\left|\Delta\theta_{CA}^{UV \mp vis}\right| \geq 50^\circ$  criterion is significantly greater than the ~5–10° variations observed. Yet, these estimates are potentially overestimates

because  $\Phi$  is also influenced by the light induced changes in surface energy. Nevertheless, these estimates are supported by recent wetting state predictions by others - see, e.g., Fig. 2(e) in [70].

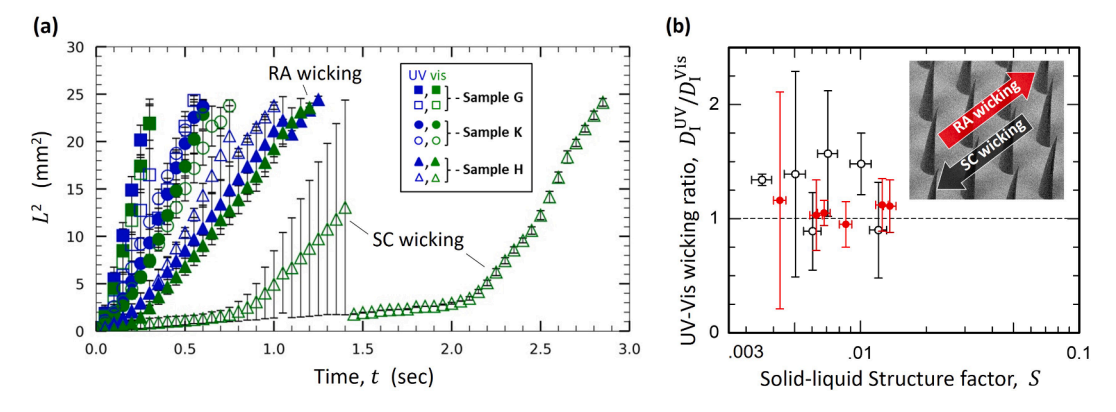


Fig. 8. Hemiwicking enhancements by UV light stimulation for a 75:25 ( $\phi = 0.75$ ) ethanol/water fluid mixture on different wicking structures (SP functionalized). (a) Effects of UV and Vis light stimulation on the vertical hemiwicking performance for different anisotropic (half-conical) SP functionalized microstructured surfaces. The results are plotted in terms of the squared distance ( $L^2$ ) traveled by the fluid's meniscus front as a function of time (t). The closed and open symbols represent the rapid ascent (RA) and sluggish climb (SC) wicking orientations, respectively. (b) Corresponding UV enhanced hemiwicking performance in terms of the interfacial diffusivity ratio ( $D_1^{UV}/D_1^{Vis}$ ) as a function of the predicted solid-liquid Structure factor S (evaluated at both the midpoint (L = 2.5 mm) and the end (L = 5 mm) of the wicking arrays). The inset image in (b) also depicts the corresponding pillar geometry orientation for SC and RA hemiwicking.

#### 3.4.2. Hemiwicking results

Along with tracking observable changes in the Cassie-Baster or Wenzel state, changes in the hemiwicking performance were also recorded. The results of our hemiwicking experiments are presented in Fig. 8. The changes in the hemiwicking performance were tracked by measuring the distance traveled by the leading edge of the wicking front as a function of time. The results indicate that, similar to what was observed with the Wenzel state, the photoisomerization of the SP will enhance the hemiwicking performance on the microstructured surfaces. For these experiments, water, ethanol, and water-ethanol mixtures were used. However, for hemiwicking to occur a fluid with an equilibrium contact angle less 50 degrees was needed. Therefore, the presented data is for a 75:25 ethanol-water mixture ( $\phi$ =0.25), where hemiwicking and hemiwicking enhancements with the tested wicking arrays were not possible, as expected, with pure water because  $\theta_{CA}^{H_2O}\gg\theta_{CA}^{Eapping}$  [64,71].

To emphasize the diffusive nature of the hemiwicking process, we plot the data in terms of the interface diffusivity  $D_I$  of the wicking front:

$$L = (D_I t)^{1/2} (10)$$

where L is the distance traveled by the leading edge of the wicking fluid,  $D_I$  is the interface diffusivity, and t is the time of travel. These results show that the dynamic surface wetting is impacted by the change in surface chemistry (or energy) due to photoisomerization. Thus, the orientation of the SP impacts both the static and dynamic surface wetting behavior. Based on these UV $\rightleftharpoons$ vis hemiwicking results, it is clear that the use of photoreactive compounds can dictate the wicking speeds in-real time beyond what can be achieved by changes in the surface microstructure alone.

Recent work on hemiwicking has derived a solution for the hemiwicking velocity in compact form as [72–74]:

$$U(L) = \frac{1}{C_{d0}} \left(\frac{\sigma}{\mu}\right) S = \frac{1}{C_{d0}} \left(\frac{\sigma}{\mu}\right) \frac{K}{L} \tag{11}$$

where U is the hemiwicking velocity,  $C_{d0}\approx 24$  is the drag coefficient in the Stokes flow regime (Re  $\ll 1$ ), S=K/L is the dimensionless solid-liquid Structure factor, K is the solid-liquid surface texture, and the surface tension to dynamic viscosity ratio  $(\sigma/\mu)$  is a capillary velocity (which represents the maximum speed for wetting a flat, dry surface). Based on equations (10)–(11) the interface diffusivity of the propagating

meniscus front is predicted as:  $D_I = \frac{2}{C_{d0}} \left( \frac{\sigma}{\mu} \right) K$ . The solid-liquid Structure factor S ties the surface chamietries of the fluid and solid (i.e. the

factor S ties the surface chemistries of the fluid and solid (i.e., the attractive solid-liquid interfacial forces) with the surface microstructure. Thus, both solid-liquid Structure factor (S) and the solid-liquid surface texture (K) couple the fluid-solid wetting behavior to the geometry/texture of the hemiwicking surface.

Past work derived the wicking/pumping force per unit wicking cell width  $(f_w \approx \sigma \kappa \frac{A_w}{s_y})$  based on a liquid meniscus curvature scaling as  $\kappa \approx h/x_0^2$ , where h is the pillar height and  $x_0$  is the measured, steady-state meniscus extension. For this work we revisited the wicking/pumping force per unit cell width based on the contemporary capillary rise problem with a meniscus curvature scaling as  $\kappa = 2\cos\left(\theta_{CA}^* + \beta\right)/s_\kappa$ , where  $\beta$  is the slant angle of the pillar walls relative to the substrate surface normal and  $s_\kappa$  is the interpillar gap separation (see the Supplementary Information, Fig. S10). As a result, a force balance between the wicking and viscous drag force  $(f_w \approx f_{C_{d0}})$  leads to the generalized solution for the solid-liquid surface texture,

$$K = \frac{2\cos(\theta_{CA}^* + \beta)}{s_x} \left[ \frac{A_w}{A_{CD}} \right] L_C \left( \frac{s_x}{\cos\alpha} - d^* \right)$$
 (12)

where  $\theta_{CA}^*$  is the equilibrium contact angle of the fluid meniscus in contact with the pillar wall,  $\frac{A_w}{A_{C_{d0}}}$  is the ratio of the pillar surface area for pumping/wicking to the pillar surface area for viscous drag per unit cell,

 $L_C$  is the characteristic length for the flow-field (Re  $= \rho U L_C/\mu$ ), and the  $(s_x/\cos\alpha - d^*)$  term accounts for packed bed limit with  $d^* = d$  for cylindrical pillars. Thus, the revised wicking model accounts for light-activated changes in the wetting behavior  $(\theta_{CA}^{\mathrm{UV} \neq \mathrm{vis}})$  and anisotropic pillar geometries ( $\beta \neq 0$ ). We note that  $\theta_{CA}^*$  used in the wicking model should be that of the flat wall (or that relative to the surface normal of pillar wall), not the apparent contact angle of the fluid with the microstructured surface.

The revised hemiwicking model is supported by a majority of the acquired UV ⇒vis hemiwicking data in Fig. 8, where, in general, the vertical hemiwicking velocities (or meniscus interface diffusivity) increases upon UV photoisomerization of the open-SP surface state. Therefore, along with the static pillar geometry and pillar spacing configuration, the dynamic state of the surface chemistry is a key metric for engineering the wetting behavior. Such transient surface-chemistry effects are crucial in areas such as thermal transport, where the real-time changes in surface chemistry (via surface oxidation and fouling at high heat fluxes) result in significant, irreversible reductions in the critcal heat flux and nucleate boiling heat transfer coefficients.

Our choice of the tested (vertical) wicking orientation is worth additional clarification - i.e., vertical hemiwicking from a fluid pool (Fig. 3(b)) as opposed to lateral (horizontal) hemiwicking from a droplet (Fig. 1(d), fluid penetration). We did test both wicking configurations. However, while we did observe UV ≠vis photoswitching of the apparent contact angles with multiple fluids in the horizontal configuration (see, Fig. 3(a) and Fig. 7), we did not observe Wenzel (or Cassie-Baxter) to hemiwicking state transitions in the horizontal configuration with the presented fluid droplets on the photoactive microstructured surfaces. Therefore, the final studies focused on vertical hemiwicking against gravity from a fluid pool to demonstrate tunability of the wicking force via photoisomerization of SP on microstructured Au substrates. In regard to the propagation dynamics of the hemiwicking front, while we were able to modulate the static and dynamic contact angle over a relatively broad range using water and ethanol-water mixtures, we did not observe significant and reproducible variations in the hemiwicking zipping dynamics (see, Supplementary Fig. S11, Fig. S12, and the Supplemental video). The corresponding zipping ratio has been derived from previous works [64-65], where the zipping ratio is also derived via an energy and mass balance on a hemiwicking configuration and is tied to a critical contact angle [65] that scales as  $\cos\theta_c = -1 + 2h/(2h + s_\kappa)$ . Also, while we demonstrated that photoisomerization of SP induces systematic modulations in the surface energy, aside from changes in the static contact angle, the cameras used in this study were unable to detect the photoinduced changes in the meniscus curvature ( $\kappa$ ). Refined studies are needed to understand the role of the photoinduced changes in  $\kappa$  and  $\nabla \kappa$ 

The present work did not observe the pursued transition from static Cassie-Baxter (or Wenzel) state to the dynamic hemiwicking state based on the photoisomerization of SP on Au microstructured surfaces. Even with the use of different microstructures, the achieved photoisomerization of SP (i.e.,  $\left|\Delta\theta_{CA}^{\text{UV} \rightleftharpoons \text{vis}}\right| \approx 5\text{--}10^\circ$ ) is not sufficient to alternate between wetting states. Moreover, these surface free energy variations do not appear to be enough to overcome the solid-fluid absorption/binding energy for wetting state alternations at timescales appropriate for most fluid dynamic processes (i.e., timescales on the order of tens of milliseconds or less). To achieve such multi-purpose surface switching (i.e., a surface that can self-wet and self-dry based on the photo-state of SP), surface free energy changes corresponding to  $\left|\Delta\theta_{CA}^{\text{UV} \rightleftharpoons \text{vis}}\right| > 30\text{--}50^\circ$  are needed. The following expression has been utilized to scale the differential surface free energy (dG) per unit length (dx) for microstructured surfaces, namely with hemiwicking [75],

$$dG = (\gamma_{SL} - \gamma_{SV})f_r(1 - \Phi)dx - \gamma \Phi dx + \gamma f_r \cos\theta dx$$
(13)

where  $f_r$  is the surface roughness factor and  $(1-\Phi)$  is the structure

fraction remaining dry. Based on what has been discussed in this study regarding the achievable changes in  $\theta_{CA}$  (or the surface free energy), it can be concluded from Eq. (13) that the overall free energy per unit length will increase with photoisomerization of the SP coating. However, despite the expected increase in the overall surface free energy per unit length (based on the photoisomerization of SP), dramatic improvements in  $\Delta \gamma$  (or  $\Delta \theta_{CA}$ ) are needed for new technologies based on the static-to-dynamic wetting state transitions discussed herein. Based on Eq. (13), such static-to-dynamic transitions will require changes in surface free energy that are much greater than the 13% achieved in this work.

In regard to future applications, while the demonstrated hemiwicking enhancements were only nominal, it still seems favorable to incorporate SP (or other photoactive compounds) in heat transfer systems such as heat pipes for actively tuning the overall heat transfer coefficient. This aspect of the design would take advantage of the additional chemically capillary action to increase or decrease the overall two-phase thermal transport. Moreover, applications based on photoactive inhibition, elastocapillary effects, and packed bed capillary tubes (wicks) seem promising based on the significant increase in solid-liquid surface area that be achieved with such systems. In principle, the performance limits of such devices can be rapidly accessed by simply measuring the photoisomerization-induced changes in the elastocapillary length or capillary gravity length.

#### 4. Conclusion

As demonstrated in this study, the use of photoactive compounds on a microstructured Au surface affects the surface wetting between the two different states. On both smooth and microstructured Au, changes in the wetting dynamics were captured upon photoisomerization of SP through the static, dynamic, and apparent contact angle  $\theta_{CA}$ . Along with  $\theta_{CA}$ , changes in the diffusion of a polar fluid wicking through a microstructured array based on the orientation of SP were also recorded. Based on the observed changes in  $\theta_{CA}$  and the interface diffusivity, the different surface energies between the two different photoisomerization states were calculated through both the Owens-Wendt and Van-Oss models. Results presented in this work give the community a better understanding of the limitations of photoreactive surface coatings for the use in a variety of applications, including self-cleaning surfaces and thermal control devices. The slight variation of wetting behavior on the photoswitchable surface presents the possibility of having microstructured gold with controllable wettability. Further optimization is needed to maximize the photoisomerization-induced changes in the surface free energy (or, in terms of photoswitching the contact angle,  $|\Delta\theta_{CA}^{\mathrm{UV} 
ightharpoonup vis}| > 30^{\circ}$ ). Such an optimization, combined with engineering the surface microstructure, will facilitate the design of photoactive fluid switches and thermal control systems.

#### CRediT authorship contribution statement

Ali Haghighat Mesbahi: Validation, Formal analysis, Investigation, Writing – original draft, Visualization. Thomas Germain: Validation, Formal analysis, Investigation, Writing – original draft, Visualization. Parth K. Patel: Conceptualization, Methodology. Shawn A. Putnam: Conceptualization, Validation, Writing – review & editing, Supervision, Funding acquisition. Karin Y. Chumbimuni-Torres: Conceptualization, Validation, Writing – review & editing, Supervision, Funding acquisition, Project administration.

#### **Declaration of Competing Interest**

The authors declare that they have no known competing financial interests or personal relationships that could have appeared to influence the work reported in this paper.

#### Acknowledgements

The authors acknowledge the National Science Foundation. This material is based on research sponsored by the National Science Foundation (Grant No. 1653396). The views and conclusions contained herein are those of the authors and should not be interpreted as necessarily representing the official policies or endorsements, either expressed or implied, of the U.S. Government (or departments thereof). Nanolithography fabrication of microstructures, as well as thin film deposition, took place at ORNL Center for Nanophase Material Sciences under User Proposal 2018-329, which is a DOE Office of Science User Facility. We would also like to thank Daniela Vulpe for grammar revisions.

#### Appendix A. Supplementary material

Supplementary data to this article can be found online at https://doi.org/10.1016/j.apsusc.2022.152924.

#### References

- T. Shimizu, T. Goda, N. Minoura, M. Takai, K. Ishihara, Super-hydrophilic silicone hydrogels with interpenetrating poly(2-methacryloyloxyethyl phosphorylcholine) networks, Biomaterials 31 (12) (2010) 3274–3280, https://doi.org/10.1016/j. biomaterials.2010.01.026.
- [2] S. Shin, J. Seo, H. Han, S. Kang, H. Kim, T. Lee, Bio-inspired extreme wetting surfaces for biomedical applications, Mater. 9 (2) (2016) 116, https://doi.org/ 10.3390/ma9020116.
- [3] X.J. Feng, L. Jiang, Design and creation of superwetting/antiwetting surfaces, Adv. Mater. 18 (23) (2006) 3063–3078, https://doi.org/10.1002/adma.200501961.
- [4] T.A. Otitoju, A.L. Ahmad, B.S. Ooi, Superhydrophilic (superwetting) surfaces: A review on fabrication and application, J. Ind. Eng. Chem. 47 (2017) 19–40, https://doi.org/10.1016/j.jiec.2016.12.016.
- [5] H.T. Phan, N. Caney, P. Marty, S. Colasson, J. Gavillet, Surface wettability control by nanocoating: the effects on pool boiling heat transfer and nucleation mechanism, Int. J. Heat Mass Transf. 52 (23–24) (2009) 5459–5471, https://doi. org/10.1016/j.ijheatmasstransfer.2009.06.032.
- [6] H. Butt, D.S. Golovko, E. Bonaccurso, On the derivation of young's equation for sessile drops: nonequilibrium effects due to evaporation, J. Phys. Chem. B 111 (19) (2007) 5277–5283, https://doi.org/10.1021/jp065348g.
- [7] R. Shuttleworth, The Surface Tension of Solids, Proc. Phys. Soc. A 63 (5) (1950) 444–457.
- [8] Y. Yuehua, T.R. Lee, Contact angle and wetting properties, Surf. Sci. Tech. 51 (2013) 3–34, https://doi.org/10.1007/978-3-642-34243-1\_1.
- [9] J. Bico, U. Thiele, D. Quéré, Wetting of textured surfaces, Colloids Surf., A 206 (1–3) (2002) 41–46, https://doi.org/10.1016/S0927-7757(02)00061-4.
- [10] D. Janssen, R.D. Palma, S. Verlaak, P. Heremans, W. Dehaen, Static solvent contact angle measurements, surface free energy and wettability determination of various self-assembled monolayers on silicon dioxide, Thin Solid Films 515 (4) (2006) 1433–1438, https://doi.org/10.1016/j.tsf.2006.04.006.
- [11] C.I. Park, H.E. Jeong, S.H. Lee, H.S. Cho, K.Y. Suh, Wetting transition and optimal design for microstructured surfaces with hydrophobic and hydrophilic materials, J. Colloid Interface Sci. 336 (1) (2009) 298–303, https://doi.org/10.1016/j. icis.2009.04.022.
- [12] N. Shardt, M.B. Bigdeli, J.A.W. Elliott, P.A. Tsai, How surfactants affect droplet wetting on hydrophobic microstructures, J. Phys. Chem. Let. 10 (23) (2019) 7510–7515, https://doi.org/10.1021/acs.jpclett.9b02802.
- [13] H. Ems, S. Ndao, Microstructure-alone induced transition from hydrophilic to hydrophobic wetting state on silicon, Appl. Surf. Sci. 339 (2015) 137–143, https://doi.org/10.1016/j.apsusc.2015.02.135.
- [14] D. Zhang, Z. Cheng, H. Kang, J. Yu, Y. Liu, L. Jiang, A smart superwetting surface with responsivity in both surface chemistry and microstructure, Angew. Chem. 130 (14) (2018) 3763–3767, https://doi.org/10.1002/ange.201800416.
- [15] H. Jo, S. Kim, H. Kim, J. Kim, M.H. Kim, Nucleate boiling performance on nano/microstructures with different wetting surfaces, Nanoscale Res. Lett. 7 (1) (2012) 242, https://doi.org/10.1186/1556-276X-7-242.
- [16] D. Murakami, H. Jinnai, A. Takahara, Wetting transition from the cassie–baxter state to the wenzel state on textured polymer surfaces, Langmuir 30 (8) (2014) 2061–2067, https://doi.org/10.1021/la4049067.
- [17] J.B. Lee, H.R. Gwon, S.H. Lee, M. Cho, Wetting transition characteristics on microstructured hydrophobic surfaces, Mat. Trans. 51 (9) (2010) 1709–1711, https://doi.org/10.2320/matertrans.W2010118.
- [18] B.S. Kim, G. Choi, D.I. Shim, K.M. Kim, H.H. Cho, Surface roughening for hemiwicking and its impact on convective boiling heat transfer, Int. J. Heat Mass Transf. 102 (2016) 1100–1107, https://doi.org/10.1016/j. iiheatmasstransfer 2016 07 008
- [19] E. Bormashenko, R. Pogreb, G. Whyman, M. Erlich, Cassie- wenzel wetting transition in vibrating drops deposited on rough surfaces: Is the dynamic cassiewenzel wetting transition a 2d or 1d affair? Langmuir 23 (12) (2007) 6501–6503, https://doi.org/10.1021/la700935x.

- [20] A.M. Peters, C. Pirat, M. Sbragaglia, B.M. Borkent, M. Wessling, D. Lohse, R.G. H. Lammertink, Cassie-Baxter to Wenzel state wetting transition: Scaling of the front velocity, Europ. Phys. J. E 29 (4) (2009) 391–397, https://doi.org/10.1140/epie/i/2009-10488-3
- [21] R.J. Vrancken, H. Kusumaatmaja, K. Hermans, A.M. Prenen, O. Pierre-Louis, C.W. M. Bastiaansen, D.J. Broer, Fully reversible transition from Wenzel to Cassie—Baxter states on corrugated superhydrophobic surfaces, Langmuir 26 (5) (2010) 3335–3341, https://doi.org/10.1021/la903091s.
- [22] R. Wendelstorf, K.H. Spitzer, J. Wendelstorf, Effect of oxide layers on spray water cooling heat transfer at high surface temperatures, Int. J. Heat Mass Transf. 51 (19–20) (2008) 4892–4901, https://doi.org/10.1016/j. ijheatmasstransfer.2008.01.033.
- [23] W. Wu, H. Bostanci, L.C. Chow, Y. Hong, M. Su, J.P. Kizito, Nucleate boiling heat transfer enhancement for water and FC-72 on titanium oxide and silicon oxide surfaces, Int. J. Heat Mass Transf. 53 (9–10) (2010) 1773–1777, https://doi.org/ 10.1016/j.ijheatmasstransfer.2010.01.013.
- [24] A.D. Manasrah, I.W. Almanassra, N.N. Marei, U.A. Al-Mubaiyedh, T. Laoui, M. A. Atieh, Surface modification of carbon nanotubes with copper oxide nanoparticles for heat transfer enhancement of nanofluids, RSC Adv. 8 (4) (2018) 1791–1802, https://doi.org/10.1039/C7RA10406E.
- [25] G.D. Crevoisier, P. Fabre, J.M. Corpart, L. Leibler, Switchable tackiness and wettability of a liquid crystalline polymer, Sci. 285 (5431) (1999) 1246–1249, https://doi.org/10.1126/science.285.5431.1246.
- [26] Q. Fu, G.V. Rama Rao, S.B. Basame, D.J. Keller, K. Artyushkova, J.E. Fulghum, G. P. López, Reversible control of free energy and topography of nanostructured surfaces, J. Am. Chem. Soc. 126 (29) (2004) 8904–8905, https://doi.org/10.1021/ia0478950.
- [27] T. Sun, G. Wang, L. Feng, B. Liu, Y. Ma, L. Jiang, D. Zhu, Reversible switching between superhydrophilicity and superhydrophobicity, Angew. Chem. Int. Ed. 43 (3) (2004) 357–360, https://doi.org/10.1002/anie.200352565.
- [28] J. Lahann, S. Mitragotri, T.-N. Tran, H. Kaido, J. Sundaram, I.S. Choi, S. Hoffer, G. A. Somorjai, R. Langer, A reversibly switching surface, Sci. 299 (5605) (2003) 371–374, https://doi.org/10.1126/science.1078933.
- [29] S. Arscott, Moving liquids with light: photoelectrowetting on semiconductors, Sci. Rep. 1 (1) (2011) 184, https://doi.org/10.1038/srep00184.
- [30] X. Yu, Z. Wang, Y. Jiang, F. Shi, X. Zhang, Reversible pH-responsive surface: From superhydrophobicity to superhydrophilicity, Adv. Mat. 17 (10) (2005) 1289–1293, https://doi.org/10.1002/adma.200401646.
- [31] S. Minko, M. Müller, M. Motornov, M. Nitschke, K. Grundke, M. Stamm, Two-level structured self-adaptive surfaces with reversibly tunable properties, J. Am. Chem. Soc. 125 (13) (2003) 3896–3900, https://doi.org/10.1021/ja0279693.
- [32] X. Luo, Z. Zhu, Y. Tian, J. You, L. Jiang, Titanium Dioxide Derived Materials with Superwettability, Catalysts 11 (4) (2021) 425, https://doi.org/10.3390/ catal11040425.
- [33] L.M. Siewierski, W.J. Brittain, S. Petrash, M.D. Foster, Photoresponsive monolayers containing in-chain azobenzene, Langmuir 12 (24) (1996) 5838–5844, https://doi. org/10.1021/la9605060.
- [34] S.K. Oh, M. Nakagawa, K. Ichimura, Photocontrol of liquid motion on an azobenzene monolayer, J. Mat. Chem. 12 (8) (2002) 2262–2269, https://doi.org/ 10.1039/B110825P
- [35] N. Delorme, J.F. Bardeau, A. Bulou, F. Poncin-Epaillard, Azobenzene-containing monolayer with photoswitchable wettability, Langmuir 21 (26) (2005) 1278–12282, https://doi.org/10.1021/ja051517y
- 12278-12282, https://doi.org/10.1021/la051517x.
  [36] W. Jiang, G. Wang, Y. He, X. Wang, Y. An, Y. Song, L. Jiang, Photo-switched wettability on an electrostatic self-assembly azobenzene monolayer, Chem. Commun. 28 (2005) 3550-3552, https://doi.org/10.1039/B504479K.
- [37] H. Ge, G. Wang, Y. He, X. Wang, Y. Song, L. Jiang, D. Zhu, Photoswitched Wettability on Inverse Opal Modified by a Self-Assembled Azobenzene Monolayer, ChemPhysChem 7 (3) (2006) 575–578, https://doi.org/10.1002/cphc.200500496.
- [38] R. Klajn, Immobilized azobenzenes for the construction of photoresponsive materials, Pure Appl. Chem. 82 (12) (2010) 2247–2279, https://doi.org/10.1351/ PAC-CON-10-09-04.
- [39] X. Pei, A. Fernandes, B. Mathy, X. Laloyaux, B. Nysten, O. Riant, A.M. Jonas, Correlation between the structure and wettability of photoswitchable hydrophilic azobenzene monolayers on silicon, Langmuir 27 (15) (2011) 9403–9412, https:// doi.org/10.1021/la201526u.
- [40] I. Vlassiouk, C.-D. Park, S.A. Vail, D. Gust, S. Smirnov, Control of nanopore wetting by a photochromic spiropyran: a light-controlled valve and electrical switch, Nano lett. 6 (5) (2006) 1013–1017, https://doi.org/10.1021/nl060313d10.1021/ nl060313d.s001.
- [41] R. Rosario, D. Gust, M. Hayes, F. Jahnke, J. Springer, A.A. Garcia, Photon-modulated wettability changes on spiropyran-coated surfaces, Langmuir 18 (21) (2002) 8062–8069, https://doi.org/10.1021/la025963l.
- [42] G. Berkovic, V. Krongauz, V. Weiss, Spiropyrans and spirooxazines for memories and switches, Chem. Rev. 100 (5) (2000) 1741–1754, https://doi.org/10.1021/ population.
- [43] H. Zhao, D. Wang, Y. Fan, M. Ren, S. Dong, Y. Zheng, Surface with Reversible Green-Light-Switched Wettability by Donor-Acceptor Stenhouse Adducts, Langmuir 34 (50) (2018) 15537–15543, https://doi.org/10.1021/acs. langmuir.8b03296.
- [44] A. Athanassiou, M.I. Lygeraki, D. Pisignano, K. Lakiotaki, M. Varda, E. Mele, C. Fotakis, R. Cingolani, S.H. Anastasiadis, Photocontrolled variations in the wetting capability of photochromic polymers enhanced by surface nanostructuring, Langmuir 22 (5) (2006) 2329–2333, https://doi.org/10.1021/la052122g.
- [45] E. Mele, D. Pisignano, M. Varda, M. Farsari, G. Filippidis, C. Fotakis, A. Athanassiou, R. Cingolani, Smart photochromic gratings with switchable

- wettability realized by green-light interferometry, Appl. Phys. Lett. 88 (20) (2006) 203124. https://doi.org/10.1063/1.2198509.
- [46] R. Klajn, Spiropyran-based dynamic materials, Chem. Soc. Rev. 43 (1) (2014) 148–184, https://doi.org/10.1039/C3CS60181A.
- [47] L. Kortekaas, W.R. Browne, The evolution of spiropyran: fundamentals and progress of an extraordinarily versatile photochrome, Chem. Soc. Rev. 48 (12) (2019) 3406–3424. https://doi.org/10.1039/C9CS00203K.
- [48] T. Germain, C. Brewer, J. Scott, S.A. Putnam, Scalable stamp printing and fabrication of hemiwicking surfaces, JoVE (J. Vis. Exp.) 142 (2018), e58546, https://doi.org/10.3791/58546.
- [49] M. Wirde, U. Gelius, L. Nyholm, Self-assembled monolayers of cystamine and cysteamine on gold studied by XPS and voltammetry, Langmuir 15 (19) (1999) 6370–6378, https://doi.org/10.1021/la9903245.
- [50] G. Grzegorz, L. Hultman, Reliable determination of chemical state in x-ray photoelectron spectroscopy based on sample-work-function referencing to adventitious carbon: resolving the myth of apparent constant binding energy of the C 1s peak, Appl. Surf. Sci. 451 (2018) 99–103, https://doi.org/10.1016/j.apsusc.2018.04.226.
- [51] V. Fernandez, N. Fairley, J. Baltrusaitis, Unraveling spectral shapes of adventitious carbon on gold using a time-resolved high-resolution X-ray photoelectron spectroscopy and principal component analysis, Appl. Surf. Sci. 538 (2021) 148031, https://doi.org/10.1016/j.apsusc.2020.148031.
- [52] J.C. Love, L.A. Estroff, J.K. Kriebel, R.G. Nuzzo, G.M. Whitesides, Self-assembled monolayers of thiolates on metals as a form of nanotechnology, Chem. Rev. 105 (4) (2005) 1103–1170, https://doi.org/10.1021/cr0300789.
- [53] E. Cooper, G.J. Leggett, Static secondary ion mass spectrometry studies of self-assembled monolayers: influence of adsorbate chain length and terminal functional group on rates of photooxidation of alkanethiols on gold, Langmuir 14 (17) (1998) 4795–4801, https://doi.org/10.1021/la9802567.
- [54] P.E. Laibinis, G.M. Whitesides, Self-assembled monolayers of n-alkanethiolates on copper are barrier films that protect the metal against oxidation by air, J. Am. Chem. Soc. 114 (23) (1992) 9022–9028, https://doi.org/10.1021/ja00049a038.
- [55] J. Huang, J.C. Hemminger, Photooxidation of thiols in self-assembled monolayers on gold, J. Am. Chem. Soc. 115 (8) (1993) 3342–3343, https://doi.org/10.1021/ ia00061a048.
- [56] M. Zharnikov, A. Küller, A. Shaporenko, E. Schmidt, W. Eck, Aromatic self-assembled monolayers on hydrogenated silicon, Langmuir 19 (11) (2003) 4682–4687, https://doi.org/10.1021/la020841e.
- [57] M. Sprik, E. Delamarche, B. Michel, U. Röthlisberger, M.L. Klein, H. Wolf, H. Ringsdorf, Structure of hydrophilic self-assembled monolayers: A combined scanning tunneling microscopy and computer simulation study, Langmuir 10 (11) (1994) 4116–4130. https://doi.org/10.1021/la00023a035.
- [58] F.M. Fowkes, Calculation of work of adhesion by pair potential summation, J. Colloid Interface Sci. 28 (3–4) (1968) 493–505, https://doi.org/10.1016/0021-9797(68)90082-9.
- [59] A. Zdziennicka, K. Szymczyk, J. Krawczyk, B. Jańczuk, Some remarks on the solid surface tension determination from contact angle measurements, Appl. Surf. Sci. 405 (2017) 88–101, https://doi.org/10.1016/j.apsusc.2017.01.068.
- [60] F. Hejda, P. Solar, J. Kousal, Surface free energy determination by contact angle measurements—a comparison of various approaches, WDS 10 (2010) 25–30.
- [61] E. Chibowski, Surface free energy of a solid from contact angle hysteresis, Adv. Colloid Interface Sci. 103 (2) (2003) 149–172, https://doi.org/10.1016/S0001-8686(02)00093-3
- [62] M. Kalin, M. Polajnar, The correlation between the surface energy, the contact angle and the spreading parameter, and their relevance for the wetting behaviour of DLC with lubricating oils, Tribol. Int. 66 (2013) 225–233, https://doi.org/ 10.1016/j.triboint.2013.05.007.
- [63] E. Rekiel, A. Zdziennicka, B. Jańczuk, Adsorption properties of rhamnolipid and ethanol at water/ethanol solution-air interface, J. Mol. Liq. 308 (2020) 113080, https://doi.org/10.1016/j.molliq.2020.113080.
- [64] C. Pirat, M. Sbragaglia, A.M. Peters, B.M. Borkent, R.G. Lammertink, M. Wessling, D. Lohse, Multiple time scale dynamics in the breakdown of superhydrophobicity, Europhys. Lett. 81 (6) (2008) 66002, https://doi.org/10.1209/0295-5075/81/ 66002.
- [65] J. Bico, C. Tordeux, D. Quéré, Rough wetting, EPL (Europhys. Lett.) 55 (2) (2001) 214–220.
- [66] E. Bormashenko, General equation describing wetting of rough surfaces, J. Colloid. Interf. Sci. 360 (1) (2011) 317–319, https://doi.org/10.1016/j.jcis.2011.04.051.
- [67] C. Ishino, K. Okumura, D. Quere, Wetting transitions on rough surfaces, Europhys. Lett. 68 (3) (2004) 419–425, https://doi.org/10.1209/epl/i2004-10206-6.
  [68] A. Bussonnière, M.B. Bigdeli, D.-Y. Chueh, Q. Liu, P. Chen, P.A. Tsai, Universal
- [68] A. Bussonnière, M.B. Bigdeli, D.-Y. Chueh, Q. Liu, P. Chen, P.A. Tsai, Universal wetting transition of an evaporating water droplet on hydrophobic micro- and nano-structures, Soft Matter 13 (5) (2017) 978–984, https://doi.org/10.1039/ c6mp02387a
- [69] D.I. Yu, H.J. Kwak, S.W. Doh, H.C. Kang, H.S. Ahn, M. Kiyofumi, H.S. Park, M. H. Kim, Wetting and evaporation phenomena of water droplets on textured surfaces, Int. J. Heat Mass Transf. 90 (2015) 191–200, https://doi.org/10.1016/j.ijheatmasstransfer.2015.06.046.
- [70] D. Kim, N.M. Nicola, M. Pugno, S. Ryu, Wetting theory for small droplets on textured solid surfaces, Sci. Rep. 6 (1) (2016) 1–8, https://doi.org/10.1038/ cop/27212
- [71] J. Bal, K.S. Manoharan, S.A. Putnam, Spatiotemporal wicking dynamics: The effects of pillar height, density, and anisotropic geometries, in: 2021 20th IEEE Intersoc. Conf. on Therm. and Thermomech. Phenom. in Electron. Syst. (iTherm), 2021, pp. 1214–1223. Doi: 10.1109/itherm51669.2021.9503162.

- [72] J. Kim, M.W. Moon, H.Y. Kim, Dynamics of hemiwicking, J. Fluid Mech. 800 (2016) 57-71, https://doi.org/10.1017/jfm.2016.386.
- [73] S.R. Krishnan, J. Bal, S.A. Putnam, A simple analytic model for predicting the wicking velocity in micropillar arrays, Sci Rep. 9 (2019) 20074, https://doi.org/ 10.1038/s41598-019-56361-7.
- [74] H. Chen, H. Zang, X. Li, Y. Zhao, Toward a better understanding of hemiwicking: A simple model to comprehensive prediction, Langmuir 35 (7) (2019) 2854–2864, https://doi.org/10.1021/acs.langmuir.8b03611.

  [75] D. Quéré, Rough ideas on wetting, Phys. A: Stat. Mech. and its Appl. 313 (1–2)
- (2002) 32-46, https://doi.org/10.1016/S0378-4371(02)01033-6.